

Nanopore-Based Measurements of Protein Size, Fluctuations, and Conformational Changes

Pradeep Waduge,[†] Rui Hu,^{§,#} Prasad Bandarkar,^{†,#} Hirohito Yamazaki,[⊥] Benjamin Cressiot,[†] Qing Zhao,[§] Paul C. Whitford,^{*,†} and Meni Wanunu^{*,†,‡,§}

[†]Department of Physics and [‡]Department of Chemistry and Chemical Biology, Northeastern University, Boston, Massachusetts 02115, United States

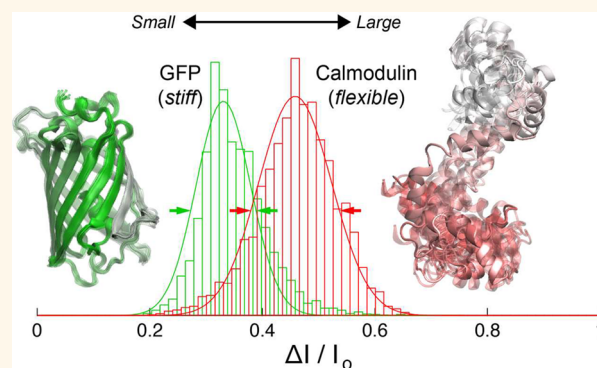
[§]State Key Laboratory for Mesoscopic Physics, School of Physics, Peking University, Beijing 100871, People's Republic of China

[⊥]Graduate School of Science and Technology, Keio University, 3-14-1 Hiyoshi, Kouhoku-ku, Yokohama, Kanagawa 223-8522, Japan

Supporting Information

ABSTRACT: Proteins are structurally dynamic macromolecules, and it is challenging to quantify the conformational properties of their native state in solution. Nanopores can be efficient tools to study proteins in a solution environment. In this method, an electric field induces electrophoretic and/or electro-osmotic transport of protein molecules through a nanopore slightly larger than the protein molecule. High-bandwidth ion current measurement is used to detect the transit of each protein molecule. First, our measurements reveal a correlation between the mean current blockade amplitude and the radius of gyration for each protein. Next, we find a correlation between the shape of the current signal amplitude distributions and the protein fluctuation as obtained from molecular dynamics simulations. Further, the magnitude of the structural fluctuations, as probed by experiments and simulations, correlates with the ratio of α -helix to β -sheet content. We highlight the resolution of our measurements by resolving two states of calmodulin, a canonical protein that undergoes a conformational change in response to calcium binding.

KEYWORDS: nanopores, electro-osmosis, ζ -potential, structural fluctuations, protein conformation



Proteins represent an important class of biomolecules in living organisms due to their diverse range of structural and functional features. Vast interest in protein structure/function relationships has spawned many techniques for probing protein structure. However, function is intricately linked to dynamic structural changes that are mediated by environmental conditions, as well as interactions with external agents such as ligands, ions, and other proteins. The advent of single-molecule methods has enabled deep insights into the dynamic aspects of biomolecules *in vitro*. Single-molecule optical methods, such as fluorescence resonance energy transfer (FRET),^{1–6} have been used to probe protein folding by detecting distinct subpopulations and protein conformational changes.^{7–13} Likewise, mechanical properties (*e.g.*, rigidity) of surface-immobilized and membrane-bound proteins have been studied using atomic force microscopy (AFM).^{14–16} However, in all of these works, the protein typically needs to be chemically modified so that it can be immobilized to a surface.

This drawback is often tedious, costly, and can potentially impact the native protein's properties.

Nanopore sensors have recently emerged as a powerful tool to probe individual molecules. A nanopore sensor is a nanometer-sized hole within an ultrathin impermeable membrane that separates two chambers, each containing electrolyte solution. Macromolecules can be driven through the pore by applying an electrical potential across the pore. Analysis of changes in the ionic current that result from pore occlusion provides information about the size of the polymer.¹⁷ While the majority of nanopore studies have primarily focused on understanding DNA transport kinetics and its implications on DNA sequencing,^{18,19} nanopores have also found use in the detection of small molecules,^{20,21} chemical reactions,^{22,23}

Received: February 20, 2017

Accepted: May 4, 2017

Published: May 4, 2017

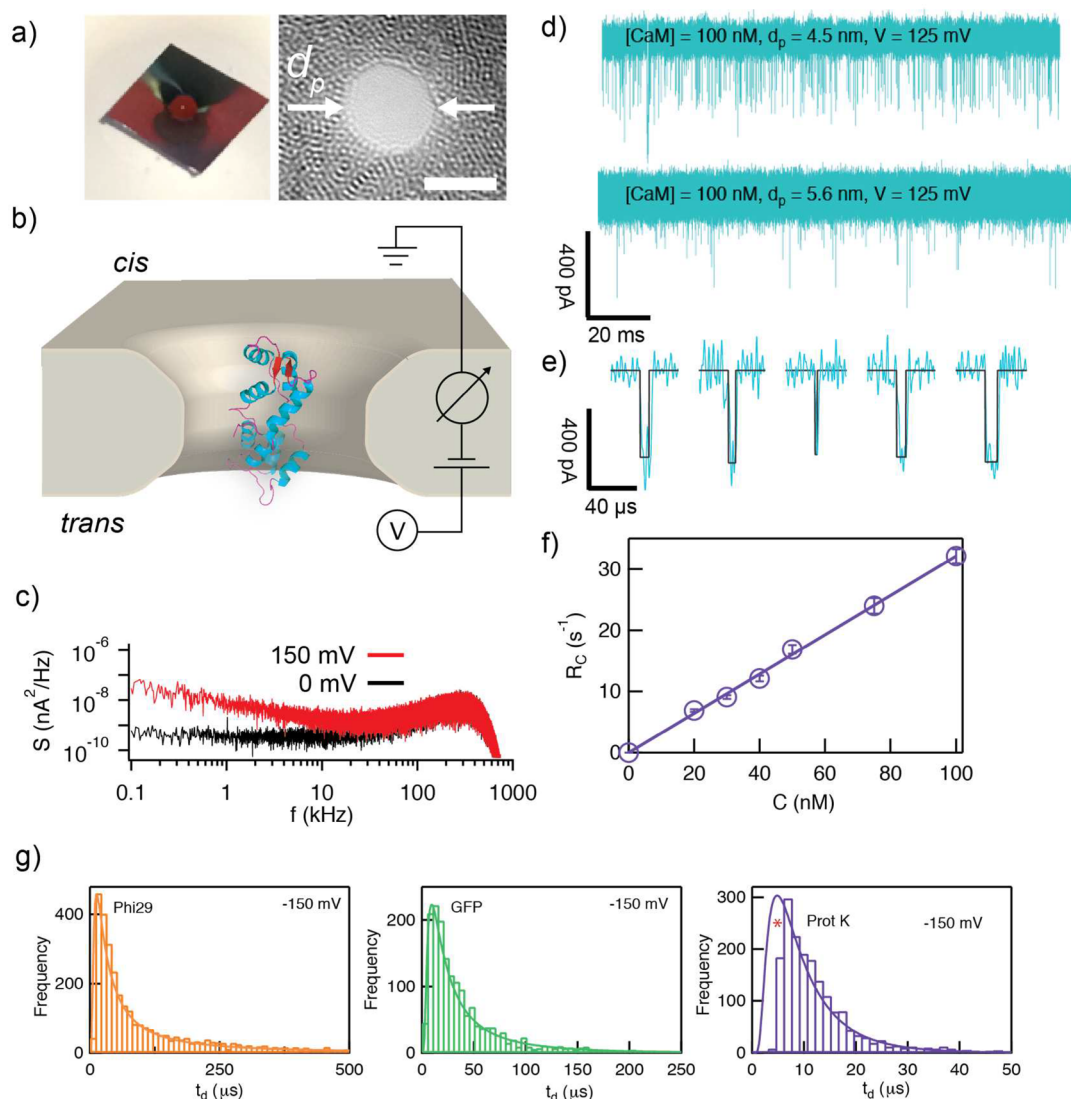


Figure 1. Nanopore experimental setup for protein detection. (a) Left: Silicon chip containing a freestanding HfO_2 membrane, after painting with a quick-curing silicone elastomer to reduce the chip's capacitance noise. Right: Bright-field TEM image of a HfO_2 pore (scale bar is 5 nm). (b) Schematic of the nanopore setup, where nanopores are fabricated in thin (<10 nm) freestanding silicon nitride (SiN) or HfO_2 membranes. Protein samples are added to the *cis* (grounded) chamber, and external bias is applied to the *trans* side of the membrane to drive protein molecules through the pore (PDB cartoon of calmodulin is shown for illustration). (c) Power spectral density plots for the pore shown in (a), buffer contains 0.4 M KCl, 10 mM Tris, 1 mM EDTA, pH 7.8. (d) Continuous ion current traces, low-pass filtered to 200 kHz, showing calmodulin transport through 4.5 and 5.6 nm diameter SiN pores. Baseline currents (I_0) were 1.35 and 1.91 nA for 4.5 and 5.6 nm diameter SiN pores, respectively. (e) Selected events extracted from the top trace in (d). (f) Capture rate *vs* concentration for proteinase K translocations through $d = 4.8$ nm and $h_{\text{eff}} = 9$ nm SiN pore, low-pass filtered at 150 kHz at $V = -150$ mV. (g) Dwell-time distributions for transport of phi29 polymerase, GFP, and ProtK through the same 5.5 nm diameter HfO_2 pore at $V = -150$ mV, along with fits to eq 1 with D_{pore} and v_d as free parameters (solid lines). Signals were low-pass filtered at 200 kHz prior to analysis. Red asterisk for ProtK distribution highlights the regime with undetected events due to bandwidth limitations. Two different SiN pores and one HfO_2 pore were used for experiments shown in this figure.

synthetic polymers,^{24,25} and proteins.^{26–31} Nanopore measurements have yielded information about protein binding to nucleic acids,³² protein size,^{33,34} folding/unfolding,^{34–39} charge,^{30,40} and protein–aptamer interactions.⁴¹ Recently, it was recognized that the use of pores that are much larger than the protein severely biases the sampling efficiency due to fast protein translocation, which results in inefficient and highly biased detection of only proteins with long residence times inside the pore.⁴² Protein transport kinetics have been slowed down by chemically linking the proteins to lipid anchors,^{43,44} from which approximate shape, volume, charge, rotational diffusion coefficient, and dipole moment of individual proteins

have been recently determined. Although information-rich, we note two factors that limit this multiparameter approach: first, only a small fraction of long-lived resistive pulses are suitable for analysis,⁴³ and second, the proteins of interest need to be bound to lipid monomers, which requires chemical modification. Label-free approaches to protein detection have required the use of pores that are slightly larger than the protein size, coupled to measurement using high-bandwidth electronics.⁴⁵ This approach has proven useful for efficient detection of protein size, as well as for identifying complexation/dimerization of very small proteins (<30 kDa).^{45–47} Specifically, in the pore size range $d_p/d_H < 1.5$, where d_H is the

protein's hydrodynamic diameter and d_p is the pore diameter, reduced protein mobilities during transport may be attributed to increased hydrodynamic drag and protein/pore interactions, which enable efficient detection.⁴⁵

In this work, we use thin and small (comparable to the size of the protein) pores composed of both silicon nitride (SiN) and hafnium oxide (HfO₂), combined with high-bandwidth amplifiers, to detect various proteins of different sizes and charge. A main advantage of HfO₂ as a material is its combined mechanical and chemical stability,^{48,49} which enables ultrathin pores with enhanced longitudinal stability to be fabricated. Ultrathin pores afford a higher signal-to-noise ratio, which allows high-bandwidth measurements, necessary for detecting small molecules like proteins whose transit times are typically fast (~microsecond time scales). While SiN of a similar geometry can be fabricated, ultrathin SiN (~5–10 nm) is prone to rapid (~hours) morphological changes and expansion, due to chemical instability and heterogeneity.^{50,51} We utilize small and ultrathin pores to demonstrate that protein size, protein fluctuations, and conformational changes can be efficiently detected *via* statistical analysis of a set of resistive pulses for a given sample. We analyze a set of different proteins that vary in charge and sizes in order to show that (1) the hydrodynamic radius of the proteins correlates with the resistive pulse signal amplitudes, (2) experimental full width at half-maximum (fwhm) values of the current signal amplitude distributions correlate well with protein fluctuation amplitudes observed in simulations, as well as exhibiting a link between protein fluctuation and β -sheet content for a given protein, and (3) conformational changes in calmodulin, which occur upon calcium ion binding, can be detected as a shift in the nanopore signal characteristics. These results highlight the potential for applications of nanopore-based analysis in label-free probing of proteins at subpicomole levels.

RESULTS AND DISCUSSION

Nanopore Experimental Setup. An optical image of our nanopore chip is shown in Figure 1a (left). The center of the silicon chip contains a freestanding ultrathin hafnium oxide (HfO₂) membrane, in which a 5.5 nm nanopore was fabricated using a transmission electron microscope (TEM). A TEM image of the pore is shown in Figure 1a (right). High-frequency electrical noise that results from a high chip capacitance was reduced by painting a quick-drying silicone elastomer close to the chip's freestanding membrane (see image in Figure 1a, left).⁵² The mounted chip is then placed in a two-compartment fluidic cell in which buffer and sample molecules can be freely exchanged, as shown in Figure 1b. Voltage is applied across the membrane using a pair of electrodes, and the resulting current is measured using a high-bandwidth amplifier. Power spectral density plots for this low-noise chip configuration are shown in Figure 1c, at either no voltage or at a typical applied voltage (V) of 150 mV. The power spectral density plots show an increased slope that corresponds to $1/f$ noise in the low-frequency regime when voltage is applied, which has been suggested to be associated with temporal charge fluctuations in the pore.⁵³ In the high-frequency regime, the PSDs overlay well as noise in this regime is dominated by the chip geometry/capacitance. The sharp drop-off in signal beginning at 300–500 kHz is due to an applied 500 kHz low-pass filter. Figure 1b also shows a protein molecule, in this case, calmodulin, in the top (*cis*) chamber, to illustrate the convention that all sample molecules are introduced to the *cis* chamber, and voltage is always applied

to the *trans* chamber. Addition of 100 nM calcium-free calmodulin (Apo-CaM) to the *cis* chamber at $V = 125$ mV yields a set of stochastic current spikes that correspond to transport of protein molecules through the pore. To demonstrate the impact of pore diameter selection on protein detection efficiency, we compare measurements for two pores with different diameters (Figure 1d), 4.5 and 5.6 nm, under the same experimental conditions. The lower CaM capture efficiency through the larger diameter pore, seen in the current traces, is a consequence of experimental limitations: protein transport is too fast under conditions of low confinement in the larger pore, resulting in many unobserved transport events. Therefore, the pore diameter must be tailored to the size of a protein for efficient detection. For consistency throughout the article, we selected pore sizes that are 1.2–1.5 times larger than the protein hydrodynamic diameter and thickness values that are in the range of 4–9 nm. Randomly selected resistive pulses that correspond to transport of individual CaM molecules through the 4.5 nm pore are shown in Figure 1e. In Figure 1f, we plot the capture rate as a function of bulk protein concentration for proteinase K (ProtK), which displays a linear relationship, as expected (for details on capture rate determination, see Figure S1 in Supporting Information).

In previous works, we⁴⁵ and others^{36,54,55} have utilized a 1D drift-diffusion model that assumes barrier-free transport to fit protein translocation dwell-time distributions

$$P(t) = (h_{\text{eff}}/4\pi D_{\text{pore}} t^3)^{1/2} e^{-(h_{\text{eff}} - v_d t)^2/4D_{\text{pore}} t} \quad (1)$$

where h_{eff} is the effective pore thickness, D_{pore} is the protein in-pore diffusion coefficient, and v_d is the protein drift velocity inside the pore. Figure 1g shows dwell-time distributions for transport of phi29 DNA polymerase (Phi29), green fluorescent protein (GFP), and proteinase K (ProtK) at $V = -150$ mV, as well as fits of the distributions to eq 1. As highlighted by the red asterisk in the distribution for ProtK, fast protein transport for ProtK (the smallest of the three proteins) results in events that are likely missed by our experimental setup ($\sim 2.5 \mu\text{s}$ for 200 kHz bandwidth). Therefore, the fastest histogram bin is ignored (masked) when fitting the experimental distributions to eq 1.⁴⁵

Pore Surface Charge Measurements. In order to understand the primary mechanism responsible for protein capture into the pore, we first characterized the pore surface charge using streaming potential measurements, analogous to the method reported by Firnkes *et al.*⁴⁰ We have designed an automated pneumatic pressure scanner that allows streaming potentials to be measured by applying pressure increments to the *cis* chamber. Two consecutive scans are shown in Figure 2a for a SiN pore. The slopes of the streaming potential *versus* pressure curves, obtained by linear fits, combined with any possible edge effects due to thin pores of aspect ratio (h/d) ~ 1 as elucidated in Mao *et al.*, yield ζ -potential values which we find to be consistently in the range of -7.9 ± 1.6 mV for SiN and -8.6 ± 0.6 mV for HfO₂ at pH 7.8 (see Figure 2b,c, respectively, and section SM6 in Supporting Information for details about the calculation).⁵⁶ The intercepts of all the curves in Figure 2b,c are slightly shifted because of small (<0.1 mV) electrode offset potentials during the experiments. However, these offsets do not affect the ζ -potential calculation.

Protein Transport Kinetics. To gain an understanding of protein transport kinetics under confinement, we report in Table 1 parameters obtained from experiments and calculations. First, we estimate the bulk diffusion coefficients (D_{bulk})

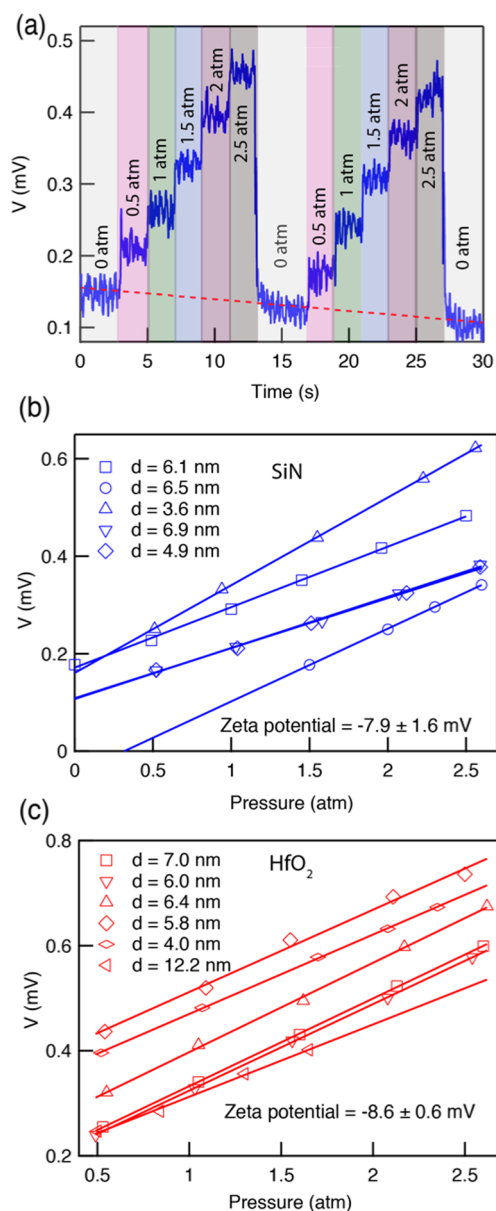


Figure 2. SiN and HfO₂ pore surface charge determination. (a) Streaming potential vs time trace for a 6.9 nm diameter SiN pore at various applied pressure ranges from 0 to 2.5 atm in 0.4 M KCl, 10 mM Tris, 1 mM EDTA, pH 7.8. Red dashed line shows slow voltage drift in the electrodes during the measurement ($100 \mu\text{V min}^{-1}$). (b) Streaming potential vs applied pressure for SiN and (c) HfO₂ pores with different diameters, as shown in the legend. As shown in the legends of the figures, we have used five different SiN pores and six different HfO₂ pores for streaming potential experiments.

of the proteins using a modified Stokes–Einstein equation (see section SMS in Supporting Information for more details)⁵⁷ and compared these with the in-pore values, D_{pore} . In agreement with our previous findings, in-pore diffusion coefficients are in stark contrast to bulk values, with a nearly 2 orders of magnitude reduction. Reduced in-pore diffusion coefficients are a result of confinement, and/or protein–pore interactions that may lead to a reduction in the effective diffusion coefficient.^{58,59} For example, this may arise from protein–pore interactions, as described previously.⁶⁰ Next, we present the protein charge at pH 7.8, q_{cal} , obtained from Poisson–Boltzmann electrostatic calculations of the folded protein.⁶¹ In the “forces” column, we

show the directions of electro-osmotic and electrophoretic velocities, with the transport direction being downward. The electro-osmotic direction (EO) is determined by the surface charge of the pore and the applied voltage, whereas the electrophoretic direction (EP) is determined by the protein charge and applied voltage. It should be noted that we have considered edge effects in our calculations by performing numerical calculations as described by Mao *et al.* (see Supporting Information SM6 and SM7 for more details).⁵⁶ It is apparent that for most of the proteins studied, the dominant contributor of transport is electro-osmotic rather than electrophoretic. By knowing the experimental drift velocities (v_d) and the electro-osmotic velocity (v_{EO}), determined analytically from the pore geometry, surface charge, and applied voltage, we can attempt to recover the protein charge (q_{exp}) by extracting the electrophoretic contribution to the velocity (see sections SM6, SM7, and SM8 in Supporting Information). We find that the estimated protein charge values do not compare well with their calculated values (see Supporting Information for estimated protein charge values). We attribute this discrepancy to an overwhelming role of electro-osmosis on transport. The large impact of electro-osmotic velocity diminishes the relative electrophoretic component in governing transport, which complicates charge calculation.

Protein Structure and Fluctuations. A deeper look into the nature of the current signals obtained from the proteins reveals several new pieces of information about the protein size and dynamics. Protein hydrodynamic radii, assuming they maintain their globular structures during transport through the pore, can be estimated from fractional current amplitude data based on^{45,62}

$$R_H \cong \frac{1}{2} [\langle \Delta I / I_0 \rangle (h_{\text{eff}} + 0.8d_p)^2 d_p^2]^{1/3} \quad (2)$$

where R_H is the protein hydrodynamic radius, d_p is the pore diameter, h_{eff} is the effective thickness of the pore, and $\langle \Delta I / I_0 \rangle$ is the mean fractional current blockade (*i.e.*, mean current blockade/open-pore current). Histograms of $\Delta I / I_0$ for three proteins at $V = -150$ mV are shown in Figure 3a. From these data, we estimated protein hydrodynamic radii by fitting the $\Delta I / I_0$ histograms to Gaussian distribution functions and using the mean values in eq 2. We then compared the experimentally obtained R_H values to the proteins’ radii of gyration, R_G (see Figure 3b, bottom). The ratio between these two quantities, $\rho = R_G / R_H$, is of physical significance as it may be related to the degree of asymmetry/anisotropy in the protein. The theoretical value for ρ is 0.775 for a hard sphere of uniform density, whereas for an oblate ellipsoid, values of ρ range from 0.875 to 0.987, and for a prolate ellipsoid, values range from 1.36 to 2.24.⁶³ We find a high degree of correlation between the two parameters R_H and R_G (see Figure 3b, bottom), with a Pearson coefficient $r = 0.82$. Moreover, the quantity ρ is close to the theoretical value for a sphere, 0.806 ± 0.09 , for all proteins tested (see Figure 3b, top), which suggests that the proteins maintain their shape integrity during transport through the pore.

In addition to identifying protein size, we next asked whether information regarding protein dynamics may be contained in the second moment of the fractional current amplitude distributions. To test this, we computed the atomic root-mean-square fluctuation (rmsf) values from simulations and plotted them against fwhm of the fractional current amplitude distributions (Figure 3d). To describe the structural fluctua-

Table 1. Summary of Transport Parameters in Our Experiments^a

protein	D_{bulk}^b	D_{pore}	q_{cal}^c (e)	forces	v_d^d	v_{EO}^e
ADK	88	0.93 ± 0.18	-9	EO↓, EP↑	0.4 ± 0.02	16.2
ADK-AP ₃ A	95	0.76 ± 0.21	-12	EO↓, EP↑	0.5 ± 0.03	16.2
GFP	84	0.54 ± 0.01	-6	EO↓, EP↑	0.2 ± 0.03	18.3
Apo-CaM	99	1.53 ± 0.34	-26	EO↑, EP↓	0.9 ± 0.04	14.4
CaCaM	96	1.30 ± 0.15	-20	EO↑, EP↓	0.3 ± 0.02	14.4
RNase A	124	2.01 ± 0.23	+3	EO↓, EP↓	1.0 ± 0.02	19.9
ProtK	87	1.01 ± 0.60	+1	EO↓, EP↓	0.7 ± 0.03	18.3
MYO	114	1.41 ± 0.11	-0.7	EO↓, EP↑	6.0 ± 0.30	14.8
Phi29	69	0.17 ± 0.02	+7	EO↓, EP↓	0.1 ± 0.02	18.3
DHFR	112	0.88 ± 0.08	+0.8	EO↓, EP↓	0.1 ± 0.01	16.0
DHFR-MTX	109	0.78 ± 0.17	-0.6	EO↓, EP↑	0.2 ± 0.02	16.0

^a D_{bulk} and D_{pore} are protein diffusion coefficients in the bulk solution and inside the pore, respectively. q_{cal} is the protein charge calculated using available models⁶¹ based on Poisson–Boltzmann electrostatic calculations. v_d and v_{EO} represent the experimentally determined protein drift velocities and numerically calculated electro-osmotic velocities, respectively. ^bCalculated from modified Stokes–Einstein model.⁵⁷ Both D_{bulk} and D_{pore} are in $\text{nm}^2 \mu\text{s}^{-1}$. ^cAt pH 7.8. ^dExtracted by fitting 1D drift-diffusion model to dwell-time distributions. ^eObtained analytically (see Supporting Information). Computed from electro-osmotic and experimental drift velocities; see Supporting Information. Both v_d and v_{EO} are in $\text{nm} \mu\text{s}^{-1}$. Eight different pores were used to obtain the data shown in the table.

tions of each protein, we calculated the rmsf for each atom and then computed the average rmsf of each residue. We then compared to the maximum residue-averaged rmsf value with the measured fwhm value (Figure 3d).

We used an all-atom structure-based model^{64,65} to describe the interactions within each protein. In a structure-based model, all bonded and nonbonded interactions are defined such that the experimentally determined (e.g., crystallographic) structure is the global potential energy minimum. Since a large population of the protein needs to populate the native ensemble in order for a structural model to be determined, the native conformation necessarily corresponds to a free-energy minimum, consistent with the construction of a structure-based model. The functional form of this potential energy is defined such that bonded covalent interactions are maintained while the nonbonded contact interactions are able to break and re-form. This allows for one to describe the structural fluctuations in the native basin while maintaining the covalent geometry of the system.^{64,66} Finally, nonspecific excluded volume interactions are included, which account for the finite size of each atom and prevent chain crossing. The functional form of the potential is described in section SM10 in Supporting Information.

The rmsf values computed from simulations have a good correlation with the fwhm of the current amplitude distributions extracted from experiments (Figure 3c; Pearson correlation coefficient, $r = 0.73$). It should be noted that CaCaM appears to be an outlier. We suggest that this may be due to the elongated shape of CaCaM, relative to the more globular shape of the other proteins. That is, it is possible that the elongated shape may allow for additional degrees of freedom to affect the second moment of the fractional current amplitude distributions. To illustrate the difference in overall conformation, we calculated the ratio of the largest and the smallest principal moments of inertia for each protein. By definition, this ratio can be greater than or equal to one, where a value of one indicates that the protein is a spherical top. This ratio was found to lie between 1 and 2 for all proteins, except for CaCaM, for which the ratio was 4.7 (see Table S2 in Supporting Information for full list of ratios). We note that sample heterogeneity can also contribute to broadening, in addition to structural fluctuations. However, whereas this might contribute to a deviation from the correlation trendline shown

in Figure 3c, the overall data suggests that structural fluctuations play a role on the observed trend.

Peticaroli *et al.* recently performed neutron scattering and light spectroscopy to systematically establish a correlation between the protein's β -sheet content and its rigidity.⁶⁷ To explore the possible relationship between β -sheet content and flexibility, we also plotted fwhm extracted from the Gaussian distribution fits for 10 different proteins against their α -helix to β -sheet ratios at $|\Delta V| = 150 \text{ mV}$ (Figure 3d). We find that the fwhm increases with increasing α/β ratio for all proteins (reduced χ -squared, $\chi_{\text{red}}^2 = 5.5$), except for myoglobin (MYO), which is a consistent outlier (two independent measurements on different nanopores are shown in Figure 3d). These variations in the fwhm of fractional current amplitude distributions for different proteins are less likely to be due to protein rotation during its transport because our amplifier's bandwidth is much slower than typical rotation times (\sim nanosecond time scales).^{68–71}

Detecting Conformational Change in Calmodulin.

Finally, we demonstrate the ability of our nanopore construct to detect conformational changes of a protein, using calmodulin as a model system. Calmodulin (PDB ID 1QXS, 3CLN, CaM: 16.7 kDa, pI 4.2)^{72,73} is a relatively small calcium-binding protein that is expressed in all eukaryotic cells and contributes in signaling pathways that regulate growth, proliferation, and movement.^{74–76} CaM comprises two homologous globular domains connected by a flexible linker, where each domain has a pair of calcium-binding motifs called EF hands, which cooperatively bind Ca^{2+} ions. Upon Ca^{2+} binding to each globular domain, interhelical angles in the EF hand motifs are altered, resulting in a conformational change between the calcium-free (Apo-CaM) to calcium-loaded forms (CaCaM; Figure 4c).^{73,77} A large conformational change in CaM upon Ca^{2+} binding results in the molecule adopting an extended and flexible conformation in which two hydrophobic patches are exposed.⁷⁸ In addition to the immediate biological significance, knowledge of CaM binding kinetics may aid the development of genetically encoded calcium sensors. CaM conformational changes and its kinetics have been studied using nuclear magnetic resonance^{79–82} and X-ray crystallography,^{73,83} both requiring high quantities of proteins. In addition, CaM structural changes upon ligand binding have also been studied

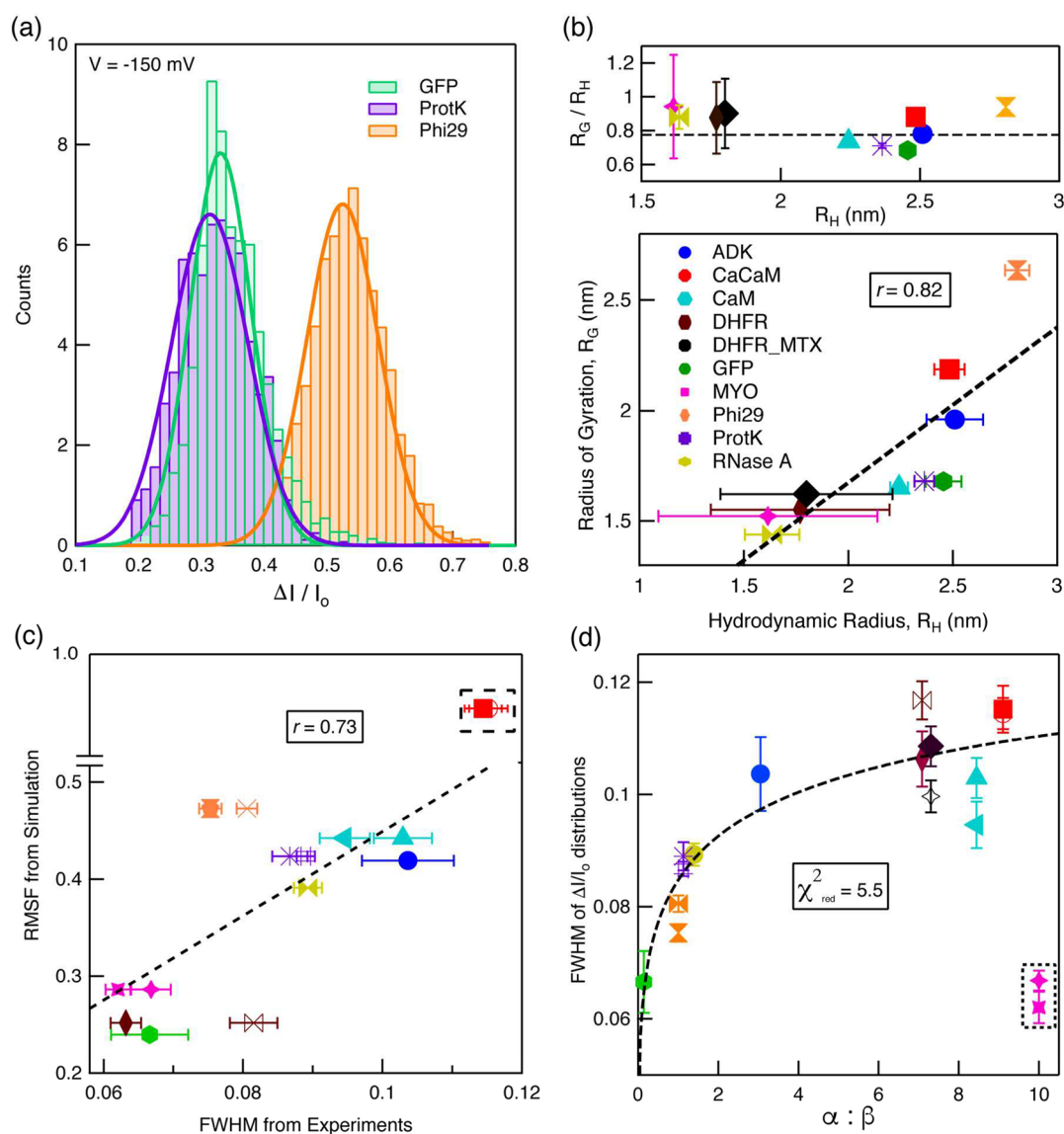


Figure 3. Protein sizing and structural fluctuations using solid-state nanopores. (a) Fractional current blockade distributions for three sample proteins (Phi29, GFP, and ProtK) at $V = -150$ mV. Solid lines represent the single Gaussian fittings to current blockade histograms, from which we extract the mean fractional blockades. (b) Top: Radius of gyration/hydrodynamic radius vs hydrodynamic radius of proteins. Dashed line represents the theoretically predicted value for shape factor, ρ ($\rho = R_G/R_H$), for globular proteins. Bottom: Radius of gyration from simulations vs estimated hydrodynamic radius of proteins. Dashed line represents the linear correlation fit to the data with $r = 0.82$ (Pearson correlation coefficient). (c) Root-mean-square fluctuation (rmsf) values from simulations vs fwhm of fractional current amplitude distributions from experiments for various proteins. Dashed line depicts the linear correlation between experimental and simulation results excluding CaCaM (a consistent outlier) with $r = 0.73$. (d) Full width at half-maximum of fractional current blockade distributions vs α -helix/ β -sheet ratio for 10 different proteins at $|\Delta V| = 150$ mV. Dashed line: empirical log-normal distribution fitting to the data omitting myoglobin (a consistent outlier). Different symbols of the same color as in (c) and (d) represent multiple data points for the same protein. Eight pores were used to obtain the data shown in this figure.

recently using second harmonic generation (SHG),^{84,85} which demands proteins to be labeled with SHG-active dyes. Moreover, SHG is only sensitive to relative orientations of proteins upon shape changes, so SHG is unable to provide detail about the change in size and structure, including the rigidity of proteins upon conformational change. In contrast, we have shown here that nanopores, which require very low sample concentrations (\sim nanomolar scale) can yield details on change in mean hydrodynamic diameter, relative charge, and rigidity of proteins upon conformational changes.

To detect a conformational change in calmodulin, we first added 100 nM of Apo-CaM to the *cis* chamber and collected

data at different voltages. We then added 0.5 mM of CaCl_2 to the sample chamber. We observe a drastic change in fractional current blockade amplitude versus dwell-time distributions toward deeper blockade amplitudes and longer dwell times upon calcium binding, as seen in Figure 4a. We attribute this change in current blockade amplitude versus dwell-time distributions to the conformational change of calmodulin from the Apo-CaM to CaCaM structure. We should note that scatterplots for Apo-CaM indicate that dwell times are sharply bandwidth-limited even at $V = 100$ mV, as indicated with a green arrow in Figure 4a, suggesting some of Apo-CaM events have dwell times that are too short for the time resolution of

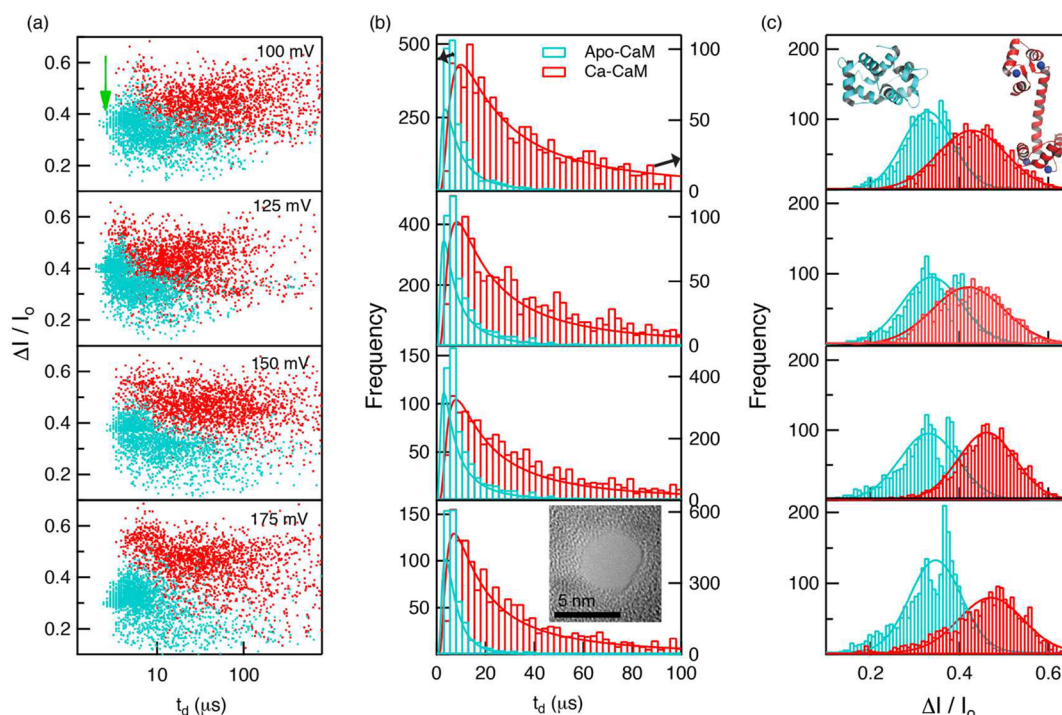


Figure 4. Discriminating Apo-CaM and CaCaM structures using solid-state nanopores. We used a 4.5 nm diameter thinned ($h_{\text{eff}} \sim 5$ nm) SiN pore in 0.4 M KCl, 10 mM Tris, 1 mM EDTA, pH 7.8; data were sampled at 4.19 MHz and low-pass filtered at 500 kHz. (a) Scatterplots of fractional current blockades vs dwell times for Apo-CaM and CaCaM at the indicated applied voltages. There are $N \sim 2,000$ events for each CaM structure at each voltage. (b) Dwell-time distributions for Apo-CaM and CaCaM along with the fits (solid lines) to the 1D drift-diffusion model (eq 1) at various voltages in the same range as in (a). Bright-field TEM image of the SiN pore used for this study is shown in the inset. (c) Fractional current amplitude distributions of two structures of CaM along with the fits to single Gaussian distribution (solid lines). Cartoons based on crystal structures of Apo-CaM and CaCaM are shown in the inset. All the data shown in this figure were obtained from one SiN pore.

our detectors. However, dwell times for CaCaM appear to be significantly less bandwidth-limited for $V < 150$ mV, indicating that Apo-CaM events are faster than CaCaM events at similar voltages. Current spikes appeared only for positive bias applied to *trans* side for both conformations (see Figure S9 in Supporting Information), indicating EP force dominates over EO flow so that CaM transport through the pore is dominated by EP force. Current–time traces also suggest that both conformations are negatively charged under our experimental conditions, 0.4 M KCl, 10 mM Tris, 1 mM EDTA, pH 7.8. Figure 4b shows dwell-time distributions for both Apo-CaM and CaCaM for various voltages range from 100 to 175 mV along with fits to the 1D drift-diffusion model (eq 1) taking both D_{pore} and v_d as free parameters. Figure 4b clearly shows that Apo-CaM translocates through the pore faster than CaCaM. Figure 4c displays distributions of fractional current amplitudes for both Apo-CaM and CaCaM in the voltage range of 100–175 mV, where CaCaM shows a deeper blockade than Apo-CaM. This suggests that CaCaM structure excludes larger cross section than Apo-CaM structure during its transport through the pore. Two distinct peaks seen for Apo-CaM at higher voltages could possibly be due to two reasons: Although Apo-CaM has a twisted four-helix bundle structure, it may retain a high degree of internal dynamics due to the highly flexible helical linker, as implicated in NMR studies.⁸⁰ Thus, while Apo-CaM is translocating through the pore, it is possible that a high voltage induces preference to different protein configurations, which result in different current blockade levels. However, since this effect dominates at high voltage, the split peak may very well be an undesirable artifact of voltage-induced

protein destabilization. Mean fractional current blockade values were extracted from fitting data to single Gaussian distributions, which were used to estimate the hydrodynamic diameter of each conformation using eq 2, as demonstrated in Figure 3b. The calculated values are in good agreement with the estimated sizes by others using different techniques.^{78,86}

As shown in Figure 5a,b, we extracted the values of D_{pore} and v_d for both states of CaM during transport through the same pore used in Figure 4 from the optimized fits of dwell times to 1D drift-diffusion model (eq 1). Drift velocities of both conformations have a linear dependence on voltage in the range of 100–175 mV. These data yield a mean electrophoretic mobility ($\bar{\mu}$) for each sample (Apo-CaM and CaCaM) by multiplying the slopes of the best-fit lines in Figure 5b by h_{eff} of the pore. We found $\bar{\mu} = 86 \pm 2 \text{ nm}^2 \mu\text{s}^{-1} \text{ V}^{-1}$ for Apo-CaM and $\bar{\mu} = 29 \pm 4 \text{ nm}^2 \mu\text{s}^{-1} \text{ V}^{-1}$ for CaCaM. According to Figure 5b, Apo-CaM translocates through the pore faster than CaCaM, which is likely due to two reasons: First, the CaCaM structure is much more flexible than the Apo-CaM molecule, which can slow down translocation. This is experimentally supported by the larger fwhm current blockade amplitude values for CaCaM than for Apo-CaM, as well as by the rmsf values obtained from simulations. Second, the net negative charge of CaCaM is lower than that for Apo-CaM due to Ca^{2+} ion binding, so that the magnitude of the EP force on CaCaM is smaller than that on Apo-CaM. In addition, as illustrated in Figure 5a, our fits yielded $\bar{D}_{\text{pore}} = 1.9 \pm 0.3 \text{ nm}^2 \mu\text{s}^{-1}$ for Apo-CaM, smaller by a factor of ~ 51 than its D_{bulk} value of $98 \text{ nm}^2 \mu\text{s}^{-1}$ and $\bar{D}_{\text{pore}} = 1.2 \pm 0.1 \text{ nm}^2 \mu\text{s}^{-1}$ for CaCaM, smaller by a factor of ~ 80 compared to its bulk value of $96 \text{ nm}^2 \mu\text{s}^{-1}$.

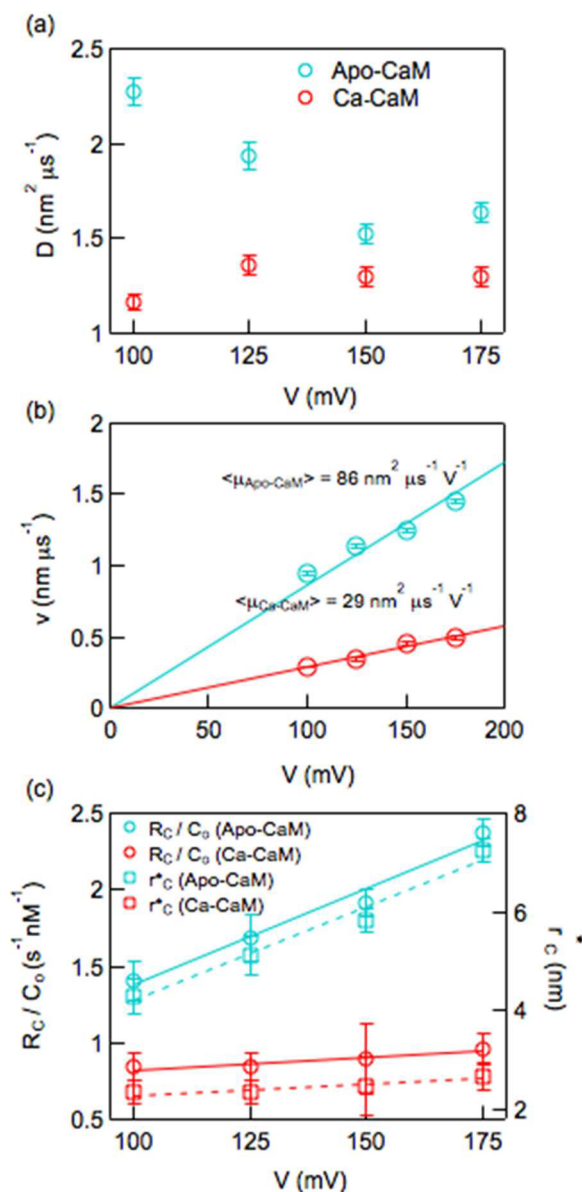


Figure 5. Transport and capture dynamics for calmodulin (a,b) diffusion coefficients (D_{pore}) and drift velocities (v_d) for Apo-CaM and CaCaM structures during transport through the same SiN pore used in Figure 4, obtained from fitting dwell times to eq 1 (Figure 4b) treating v_d and D_{pore} as free parameters, respectively. (c) Normalized capture rates and corresponding effective capture radii (r^*) for Apo-CaM and CaCaM. These data are obtained from the same SiN pore used for Figure 4.

Calmodulin Capture. In addition to discriminating between two conformations *via* in-pore drift velocities and diffusion coefficients, these parameters should also be sensitive to a change in the relative charge of the two protein forms. The difference in net charge of the two forms of calmodulin can be detected using protein capture rates, where the diffusion-drift model can be used to explain protein capture through a solid-state nanopore. A diffusion-drift model can approximate the flux of a protein, J , that enters into an absorbing pore⁸⁷

$$J = R_C / C_0 = -D_{\text{bulk}} \nabla C / C_0 + \mu E(r) \quad (3)$$

where R_C is the measured capture rate, C_0 is the bulk protein concentration in free buffer, D_{bulk} is the bulk diffusion

coefficient of the protein, ∇C is the protein concentration gradient, μ is the electrophoretic mobility of the protein, and $E(r)$ is the electric field as a function of distance from the pore. The first term in eq 3 characterizes the protein diffusion under concentration gradient, and the second term characterizes the protein drift under bias. Whereas the diffusion term dominates under low-field conditions (*i.e.*, low-bias or no-bias voltage), the drift term dominates under high-bias voltage, which is typical under nanopore experimental conditions. Therefore, protein capture rate under electric-field-driven nanopore conditions should linearly increase with voltage as well as with protein concentration. As is commonly done, we extract R_C values from single-exponential decay fits to our first arrival time distributions.⁸⁸

The normalized flux (J) of Apo-CaM and CaCaM as a function of applied voltage is presented in Figure 5c. We outline two main observations: First, the normalized flux of Apo-CaM is consistently larger than the flux of CaCaM. Second, whereas the flux for Apo-CaM increases with the applied voltage, for CaCaM, we observe a voltage-independent flux. To describe protein capture, we calculate the effective protein capture radius, r_c^* , using the Smoluchowski rate equation,⁸⁹ $J = 2\pi D_{\text{bulk}} r_c^*$, where r is the effective radius of an absorbing hemisphere that extends from the pore mouth and D_{bulk} is the protein bulk diffusion coefficient, which can be estimated using available models.⁵⁷ Based on these calculations, the effective capture radius (r_c^*) for each molecule is also plotted against applied voltage in Figure 5c. We rationalize the stark difference in capture *versus* voltage for the two molecules by considering the net charge of the two forms of calmodulin in solution: as free calmodulin (Apo-CaM) has a more negative charge than the calcium-bound form (CaCaM), electrophoresis of the molecule governs its capture behavior. In contrast, for the less negative charged CaCaM, electro-osmosis and electrophoresis, which have equal and opposite effects on capture into the pore, resulting in a voltage-insensitive behavior. To rule out the possibility that calcium may impact the pore walls, thereby affecting electro-osmosis-induced protein capture, we have performed control experiments with ProtK and ProtK+Ca, which confirm that calcium does not impact capture (see section SM12 in Supporting Information).

CONCLUSIONS

We have used here a low-noise nanopore platform to study the transport of proteins in their native state. For both silicon nitride and hafnium oxide pores, a negative surface charge induces significant electro-osmosis that allows efficient protein capture, irrespective of the protein charge in solution. By tailoring the pore geometry, we have efficiently detected protein molecules at subpicomole levels. While electro-osmosis makes protein charge calculation difficult to obtain, we extracted rich information on protein behavior by analyzing protein translocation statistics. First, the experimentally obtained hydrodynamic radii of proteins correlate well to the computed radii of gyrations of proteins from PDB coordinates. Next, we find that structural flexibility of the proteins can be gauged, with evidence for this coming from a clear correlation between fwhm of fractional current amplitude distributions and rmsf values extracted from structure-based simulations. Moreover, as previously found with neutron scattering measurements, increased β -sheet content, as compared with the α -helix content, correlates well with protein rigidity. Finally, we demonstrated that solid-state nanopores can be used to detect

a conformational change in a model protein, calmodulin. We find a marked difference in dwell time and current blockade statistics between the calcium-loaded structure of calmodulin (CaCaM) and the calcium-free structure (Apo-CaM). To the best of our knowledge, this is the first time that solid-state nanopores have been used to measure protein fluctuations (for example, rigidity) and detect conformational changes induced by ligand binding. We therefore believe that this study will establish solid-state nanopore sensors as a valuable tool for evaluating the impact of various ligands on protein size, conformation, and flexibility.

EXPERIMENTAL SECTION

Experimental Setup. Nanopores were fabricated in 4–9 nm thick SiN and crystalline HfO₂ membranes using previously reported methods.^{90,91} Nanopores were cleaned with hot piranha (3:1 H₂SO₄/H₂O₂), followed by hot deionized water before each experiment. After being dried under vacuum, nanopore chips were assembled in a custom PTFE cell equipped with Ag/AgCl electrodes, and quick-curing silicone elastomer was applied between the chip and the cell to seal the device and thereby reduce the capacitive noise. We introduced 0.4 M KCl, 1 mM EDTA, and 10 mM Tris-buffered to pH 7.8 as an electrolyte solution onto both sides of the chip. Proteins were always added to the *cis* chamber and thoroughly mixed to the indicated final concentrations. ProtK, Phi29, and RNase A samples were purchased from New England BioLabs (Ipswich, MA) or Thermo Scientific (Waltham, MA). Calmodulin and DHFR were purchased from Ocean Biologics and BioVision, respectively. The syntheses of green fluorescent protein and adenylate kinase (ADK) were elucidated by Thor *et al.*⁹² and Wolf-Watz *et al.*,⁹³ respectively. All experiments were carried out at ambient temperature. For control experiments with DNA, 1000 bp DNA (Fermentas NoLimits, Thermo Scientific) was added to the *cis* chamber to final concentration of 500 nM.

Data Collection and Processing. Nanopore current data were digitally acquired at a rate of 4.17 MHz using a Chimera instruments VC100 and low-pass filtered at indicated frequency to gain an improved signal-to-noise ratio for better event detection. The key parameters were extracted from the current readouts using Python, custom software written in the Wanunu lab (<https://github.com/rhenley/Pyth-Ion/>). The key parameters included the dwell time, t_d , which is the time for single-protein molecule to pass through the pore; the current blockade, ΔI , which is the mean current excluded from the pore by the analyte; and interevent time, dt , from which protein capture rates were computed.

ASSOCIATED CONTENT

Supporting Information

The Supporting Information is available free of charge on the ACS Publications website at DOI: 10.1021/acsnano.7b01212.

Additional information regarding protein capture rates calculation, dwell-time distributions, protein diffusion coefficients, ζ -potential calculations, electro-osmotic flow estimation, protein structural fluctuations, structure-based model, and calmodulin conformational change current traces (PDF)

AUTHOR INFORMATION

Corresponding Authors

*E-mail: p.whitford@neu.edu.

*E-mail: wanunu@neu.edu.

ORCID

Meni Wanunu: 0000-0002-9837-0004

Author Contributions

#R.H. and P.B. contributed equally.

Notes

The authors declare no competing financial interest.

ACKNOWLEDGMENTS

We acknowledge M. Alibakhshi for his assistance with electro-osmotic analysis, and M. Muthukumar for helpful discussions and assistance with the manuscript. We also want to acknowledge B. Salna, A. Benabbas, Y. Chishti, and L. Makowski for providing various protein samples. This work was supported by the National Science Foundation (NSF), Grant Nos. MCB-1645671 (M.W.) and MCB-1350312 (P.C.W.), and the National Natural Science Foundation of China (NSFC), Grant Nos. 51622201, 61571015 (Q.Z.).

REFERENCES

- (1) Schuler, B.; Eaton, W. A. Protein Folding Studied by Single-Molecule FRET. *Curr. Opin. Struct. Biol.* **2008**, *18*, 16–26.
- (2) Deniz, A. A.; Laurence, T. A.; Belgere, G. S.; Dahan, M.; Martin, A. B.; Chemla, D. S.; Dawson, P. E.; Schultz, P. G.; Weiss, S. Single-Molecule Protein Folding: Diffusion Fluorescence Resonance Energy Transfer Studies of the Denaturation of Chymotrypsin Inhibitor 2. *Proc. Natl. Acad. Sci. U. S. A.* **2000**, *97*, 5179–5184.
- (3) Kremers, G.-J.; Goedhart, J.; van Munster, E. B.; Gadella, T. W. Cyan and Yellow Super Fluorescent Proteins with Improved Brightness, Protein Folding, and FRET Förster Radius. *Biochemistry* **2006**, *45*, 6570–6580.
- (4) Merchant, K. A.; Best, R. B.; Louis, J. M.; Gopich, I. V.; Eaton, W. A. Characterizing the Unfolded States of Proteins using Single-Molecule FRET Spectroscopy and Molecular Simulations. *Proc. Natl. Acad. Sci. U. S. A.* **2007**, *104*, 1528–1533.
- (5) Haas, E. The Study of Protein Folding and Dynamics by Determination of Intramolecular Distance Distributions and Their Fluctuations Using Ensemble and Single-Molecule FRET Measurements. *ChemPhysChem* **2005**, *6*, 858–870.
- (6) Nguyen, A. W.; Daugherty, P. S. Evolutionary Optimization of Fluorescent Proteins for Intracellular FRET. *Nat. Biotechnol.* **2005**, *23*, 355–360.
- (7) Truong, K.; Ikura, M. The Use of FRET Imaging Microscopy to Detect Protein–Protein Interactions and Protein Conformational Changes in Vivo. *Curr. Opin. Struct. Biol.* **2001**, *11*, 573–578.
- (8) Heyduk, T. Measuring Protein Conformational Changes by FRET/LRET. *Curr. Opin. Biotechnol.* **2002**, *13*, 292–296.
- (9) Wallrabe, H.; Periasamy, A. Imaging Protein Molecules Using FRET and FLIM Microscopy. *Curr. Opin. Biotechnol.* **2005**, *16*, 19–27.
- (10) Kajihara, D.; Abe, R.; Iijima, I.; Komiyama, C.; Sisido, M.; Hohsaka, T. FRET Analysis of Protein Conformational Change Through Position-Specific Incorporation of Fluorescent Amino Acids. *Nat. Methods* **2006**, *3*, 923–929.
- (11) Corry, B.; Rigby, P.; Liu, Z.-W.; Martinac, B. Conformational Changes Involved in MscL Channel Gating Measured Using FRET Spectroscopy. *Biophys. J.* **2005**, *89*, L49–L51.
- (12) Chung, H. S.; Eaton, W. A. Single-Molecule Fluorescence Probes Dynamics of Barrier Crossing. *Nature* **2013**, *502*, 685–688.
- (13) Hanson, J. A.; Duderstadt, K.; Watkins, L. P.; Bhattacharyya, S.; Brokaw, J.; Chu, J.-W.; Yang, H. Illuminating the Mechanistic Roles of Enzyme Conformational Dynamics. *Proc. Natl. Acad. Sci. U. S. A.* **2007**, *104*, 18055–18060.
- (14) Moore, S. W.; Roca-Cusachs, P.; Sheetz, M. P. Stretchy Proteins on Stretchy Substrates: the Important Elements of Integrin-Mediated Rigidity Sensing. *Dev. Cell* **2010**, *19*, 194–206.
- (15) Afrin, R.; Alam, M. T.; Ikai, A. Pretransition and Progressive Softening of Bovine Carbonic Anhydrase II as Probed by Single Molecule Atomic Force Microscopy. *Protein Sci.* **2005**, *14*, 1447–1457.
- (16) Ikai, A.; Afrin, R.; Sekiguchi, H. Pulling and Pushing Protein Molecules by AFM. *Curr. Nanosci.* **2007**, *3*, 17–29.
- (17) Howorka, S.; Siwy, Z. Nanopore Analytics: Sensing of Single Molecules. *Chem. Soc. Rev.* **2009**, *38*, 2360–2384.

- (18) Branton, D.; Deamer, D. W.; Marziali, A.; Bayley, H.; Benner, S. A.; Butler, T.; Di Ventra, M.; Garaj, S.; Hibbs, A.; Huang, X.; et al. The Potential and Challenges of Nanopore Sequencing. *Nat. Biotechnol.* **2008**, *26*, 1146–1153.
- (19) Carson, S.; Wanunu, M. Challenges in DNA Motion Control and Sequence Readout Using Nanopore Devices. *Nanotechnology* **2015**, *26*, 074004.
- (20) Movileanu, L.; Cheley, S.; Bayley, H. Partitioning of Individual Flexible Polymers into a Nanoscopic Protein Pore. *Biophys. J.* **2003**, *85*, 897–910.
- (21) Braha, O.; Gu, L.-Q.; Zhou, L.; Lu, X.; Cheley, S.; Bayley, H. Simultaneous Stochastic Sensing of Divalent Metal Ions. *Nat. Biotechnol.* **2000**, *18*, 1005–1007.
- (22) Lee, J.; Bayley, H. Semisynthetic Protein Nanoreactor for Single-Molecule Chemistry. *Proc. Natl. Acad. Sci. U. S. A.* **2015**, *112*, 13768–13773.
- (23) Robertson, J. W.; Rodrigues, C. G.; Stanford, V. M.; Rubinson, K. A.; Krasilnikov, O. V.; Kasianowicz, J. J. Single-Molecule Mass Spectrometry in Solution Using a Solitary Nanopore. *Proc. Natl. Acad. Sci. U. S. A.* **2007**, *104*, 8207–8211.
- (24) Gibrat, G.; Pastoriza-Gallego, M.; Thiebot, B.; Breton, M.-F.; Auvray, L.; Pelta, J. Polyelectrolyte Entry and Transport Through an Asymmetric α -hemolysin Channel. *J. Phys. Chem. B* **2008**, *112*, 14687–14691.
- (25) Murphy, R. J.; Muthukumar, M. Threading Synthetic Polyelectrolytes Through Protein Pores. *J. Chem. Phys.* **2007**, *126*, 051101.
- (26) Siwy, Z.; Trofin, L.; Kohli, P.; Baker, L. A.; Trautmann, C.; Martin, C. R. Protein Biosensors Based on Biofunctionalized Conical Gold Nanotubes. *J. Am. Chem. Soc.* **2005**, *127*, 5000–5001.
- (27) Sexton, L. T.; Horne, L. P.; Sherrill, S. A.; Bishop, G. W.; Baker, L. A.; Martin, C. R. Resistive-Pulse Studies of Proteins and Protein/Antibody Complexes Using a Conical Nanotube Sensor. *J. Am. Chem. Soc.* **2007**, *129*, 13144–13152.
- (28) Han, A.; Schürmann, G.; Mondin, G.; Bitterli, R. A.; Hegelbach, N. G.; de Rooij, N. F.; Staufer, U. Sensing Protein Molecules Using Nanofabricated Pores. *Appl. Phys. Lett.* **2006**, *88*, 093901.
- (29) Han, A.; Creus, M.; Schürmann, G.; Linder, V.; Ward, T. R.; de Rooij, N. F.; Staufer, U. Label-Free Detection of Single Protein Molecules and Protein-Protein Interactions Using Synthetic Nanopores. *Anal. Chem.* **2008**, *80*, 4651–4658.
- (30) Fologea, D.; Ledden, B.; McNabb, D. S.; Li, J. Electrical Characterization of Protein Molecules by a Solid-State Nanopore. *Appl. Phys. Lett.* **2007**, *91*, 053901.
- (31) Sexton, L. T.; Mukaibo, H.; Katira, P.; Hess, H.; Sherrill, S. A.; Horne, L. P.; Martin, C. R. An Adsorption-Based Model for Pulse Duration in Resistive-Pulse Protein Sensing. *J. Am. Chem. Soc.* **2010**, *132*, 6755–6763.
- (32) Smeets, R.; Kowalczyk, S.; Hall, A.; Dekker, N.; Dekker, C. Translocation of RecA-Coated Double-Stranded DNA Through Solid-State Nanopores. *Nano Lett.* **2009**, *9*, 3089–3095.
- (33) Ledden, B.; Fologea, D.; Talaga, D. S.; Li, J. Sensing Single Protein Molecules with Solid-State Nanopores. In *Nanopores*; Springer: Berlin, 2011; pp 129–150.
- (34) Li, J.; Fologea, D.; Rollings, R.; Ledden, B. Characterization of Protein Unfolding with Solid-State Nanopores. *Protein Pept. Lett.* **2014**, *21*, 256–265.
- (35) Oukhaled, A.; Cressiot, B.; Bacri, L.; Pastoriza-Gallego, M.; Betton, J.-M.; Bourhis, E.; Jede, R.; Gierak, J.; Auvray, L.; Pelta, J. Dynamics of Completely Unfolded and Native Proteins Through Solid-State Nanopores as a Function of Electric Driving Force. *ACS Nano* **2011**, *5*, 3628–3638.
- (36) Talaga, D. S.; Li, J. Single-Molecule Protein Unfolding in Solid State Nanopores. *J. Am. Chem. Soc.* **2009**, *131*, 9287–9297.
- (37) Freedman, K. J.; Haq, S. R.; Edel, J. B.; Jemth, P.; Kim, M. J. Single Molecule Unfolding and Stretching of Protein Domains Inside a Solid-State Nanopore by Electric Field. *Sci. Rep.* **2013**, *3*, 1638.
- (38) Freedman, K. J.; Jürgens, M.; Prabhu, A.; Ahn, C. W.; Jemth, P.; Edel, J. B.; Kim, M. J. Chemical, Thermal, and Electric Field Induced Unfolding of Single Protein Molecules Studied Using Nanopores. *Anal. Chem.* **2011**, *83*, 5137–5144.
- (39) Cressiot, B.; Oukhaled, A.; Patriarche, G.; Pastoriza-Gallego, M.; Betton, J.-M.; Auvray, L. C.; Muthukumar, M.; Bacri, L.; Pelta, J. Protein Transport Through a Narrow Solid-State Nanopore at High Voltage: Experiments and Theory. *ACS Nano* **2012**, *6*, 6236–6243.
- (40) Firnkes, M.; Pedone, D.; Knezevic, J.; Döblinger, M.; Rant, U. Electrically Facilitated Translocations of Proteins Through Silicon Nitride Nanopores: Conjoint and Competitive Action of Diffusion, Electrophoresis, and Electroosmosis. *Nano Lett.* **2010**, *10*, 2162–2167.
- (41) Niedzwiecki, D. J.; Iyer, R.; Borer, P. N.; Movileanu, L. Sampling a Biomarker of the Human Immunodeficiency Virus Across a Synthetic Nanopore. *ACS Nano* **2013**, *7*, 3341–3350.
- (42) Plesa, C.; Kowalczyk, S. W.; Zinsmeester, R.; Grosberg, A. Y.; Rabin, Y.; Dekker, C. Fast Translocation of Proteins Through Solid State Nanopores. *Nano Lett.* **2013**, *13*, 658–663.
- (43) Yusko, E. C.; Bruhn, B. R.; Eggenberger, O. M.; Houghtaling, J.; Rollings, R. C.; Walsh, N. C.; Nandivada, S.; Pindrus, M.; Hall, A. R.; Sept, D.; et al. Real-Time Shape Approximation and Fingerprinting of Single Proteins Using a Nanopore. *Nat. Nanotechnol.* **2016**, *12*, 360.
- (44) Yusko, E. C.; Johnson, J. M.; Majd, S.; Prangkio, P.; Rollings, R. C.; Li, J.; Yang, J.; Mayer, M. Controlling Protein Translocation Through Nanopores with Bio-Inspired Fluid Walls. *Nat. Nanotechnol.* **2011**, *6*, 253–260.
- (45) Larkin, J.; Henley, R. Y.; Muthukumar, M.; Rosenstein, J. K.; Wanunu, M. High-Bandwidth Protein Analysis Using Solid-State Nanopores. *Biophys. J.* **2014**, *106*, 696–704.
- (46) Nir, I.; Huttner, D.; Meller, A. Direct Sensing and Discrimination among Ubiquitin and Ubiquitin Chains Using Solid-State Nanopores. *Biophys. J.* **2015**, *108*, 2340–2349.
- (47) Niedzwiecki, D. J.; Lanci, C. J.; Shemer, G.; Cheng, P. S.; Saven, J. G.; Drndic, M. Observing Changes in the Structure and Oligomerization State of a Helical Protein Dimer Using Solid-State Nanopores. *ACS Nano* **2015**, *9*, 8907–8915.
- (48) Nielsen, R. H. Hafnium and Hafnium Compounds. *Kirk-Othmer Encyclopedia of Chemical Technology*; John Wiley & Sons, Inc.: Hoboken, NJ, 2000.
- (49) Tapily, K.; Jakes, J. E.; Stone, D.; Shrestha, P.; Gu, D.; Baumgart, H.; Elmstafa, A. Nanoindentation Investigation of HfO₂ and Al₂O₃ Films Grown by Atomic Layer Deposition. *J. Electrochem. Soc.* **2008**, *155*, H545–H551.
- (50) Merchant, C. A.; Healy, K.; Wanunu, M.; Ray, V.; Peterman, N.; Bartel, J.; Fischbein, M. D.; Venta, K.; Luo, Z.; Johnson, A. C.; et al. DNA Translocation Through Graphene Nanopores. *Nano Lett.* **2010**, *10*, 2915–2921.
- (51) Venta, K.; Shemer, G.; Puster, M.; Rodriguez-Manzo, J. A.; Balan, A.; Rosenstein, J. K.; Shepard, K.; Drndic, M. Differentiation of Short, Single-Stranded DNA Homopolymers in Solid-State Nanopores. *ACS Nano* **2013**, *7*, 4629–4636.
- (52) Tabard-Cossa, V.; Trivedi, D.; Wiggin, M.; Jetha, N. N.; Marziali, A. Noise Analysis and Reduction in Solid-State Nanopores. *Nanotechnology* **2007**, *18*, 305505.
- (53) Hoogerheide, D. P.; Garaj, S.; Golovchenko, J. A. Probing Surface Charge Fluctuations with Solid-State Nanopores. *Phys. Rev. Lett.* **2009**, *102*, 256804.
- (54) Li, J.; Talaga, D. S. The Distribution of DNA Translocation Times in Solid-State Nanopores. *J. Phys.: Condens. Matter* **2010**, *22*, 454129.
- (55) Ling, D. Y.; Ling, X. S. On the Distribution of DNA Translocation Times in Solid-State Nanopores: an Analysis Using Schrödinger's First-Passage-Time Theory. *J. Phys.: Condens. Matter* **2013**, *25*, 375102.
- (56) Mao, M.; Sherwood, J.; Ghosal, S. Electro-Osmotic Flow Through a Nanopore. *J. Fluid Mech.* **2014**, *749*, 167–183.
- (57) He, L.; Niemeier, B. A Novel Correlation for Protein Diffusion Coefficients Based on Molecular Weight and Radius of Gyration. *Biotechnol. Prog.* **2003**, *19*, 544–548.
- (58) Zwanzig, R. Diffusion in a Rough Potential. *Proc. Natl. Acad. Sci. U. S. A.* **1988**, *85*, 2029–2030.

- (59) Bryngelson, J. D.; Wolynes, P. G. Intermediates and Barrier Crossing in a Random Energy Model (with Applications to Protein Folding). *J. Phys. Chem.* **1989**, *93*, 6902–6915.
- (60) Niedzwiecki, D. J.; Grazul, J.; Movileanu, L. Single-Molecule Observation of Protein Adsorption onto an Inorganic Surface. *J. Am. Chem. Soc.* **2010**, *132*, 10816–10822.
- (61) Dolinsky, T. J.; Nielsen, J. E.; McCammon, J. A.; Baker, N. A. PDB2PQR: an Automated Pipeline for the Setup of Poisson–Boltzmann Electrostatics Calculations. *Nucleic Acids Res.* **2004**, *32*, W665–W667.
- (62) DeBlois, R.; Bean, C. Counting and Sizing of Submicron Particles by the Resistive Pulse Technique. *Rev. Sci. Instrum.* **1970**, *41*, 909–916.
- (63) Burchard, W. Static and Dynamic Light Scattering from Branched Polymers and Biopolymers. In *Light Scattering from Polymers*; Springer: Berlin, 1983; pp 1–124.
- (64) Whitford, P. C.; Noel, J. K.; Gosavi, S.; Schug, A.; Sanbonmatsu, K. Y.; Onuchic, J. N. An All-Atom Structure-Based Potential for Proteins: Bridging Minimal Models with All-Atom Empirical Force-fields. *Proteins: Struct., Funct., Genet.* **2009**, *75*, 430–441.
- (65) Noel, J. K.; Levi, M.; Raghunathan, M.; Lammert, H.; Hayes, R. L.; Onuchic, J. N.; Whitford, P. C. SMOG 2: A Versatile Software Package for Generating Structure-Based Models. *PLoS Comput. Biol.* **2016**, *12*, e1004794.
- (66) Whitford, P. C.; Geggier, P.; Altman, R. B.; Blanchard, S. C.; Onuchic, J. N.; Sanbonmatsu, K. Y. Accommodation of Aminoacyl-tRNA into the Ribosome Involves Reversible Excursions along Multiple Pathways. *RNA* **2010**, *16*, 1196–1204.
- (67) Peticaroli, S.; Nickels, J. D.; Ehlers, G.; O'Neill, H.; Zhang, Q.; Sokolov, A. P. Secondary Structure and Rigidity in Model Proteins. *Soft Matter* **2013**, *9*, 9548–9556.
- (68) Rosenstein, J. K.; Wanunu, M.; Merchant, C. A.; Drndic, M.; Shepard, K. L. Integrated Nanopore Sensing Platform with Sub-Microsecond Temporal Resolution. *Nat. Methods* **2012**, *9*, 487–492.
- (69) Garcia de la Torre, J.; Huertas, M.; Carrasco, B. HYDRONMR: Prediction of NMR Relaxation of Globular Proteins from Atomic-Level Structures and Hydrodynamic Calculations. *J. Magn. Reson.* **2000**, *147*, 138–146.
- (70) Orekhov, V. Y.; Korzhnev, D. M.; Pervushin, K. V.; Hoffmann, E.; Arseniev, A. S. Sampling of Protein Dynamics in Nanosecond Time Scale by 15N NMR Relaxation and Self-Diffusion Measurements. *J. Biomol. Struct. Dyn.* **1999**, *17*, 157–174.
- (71) Loman, A.; Gregor, I.; Stutz, C.; Mund, M.; Enderlein, J. Measuring Rotational Diffusion of Macromolecules by Fluorescence Correlation Spectroscopy. *Photochem. Photobiol. Sci.* **2010**, *9*, 627–636.
- (72) Watterson, D. M.; Sharief, F.; Vanaman, T. The Complete Amino Acid Sequence of the Ca²⁺-Dependent Modulator Protein (Calmodulin) of Bovine Brain. *J. Biol. Chem.* **1980**, *255*, 962–975.
- (73) Chattopadhyaya, R.; Meador, W. E.; Means, A. R.; Quiocho, F. A. Calmodulin Structure Refined at 1.7 Å Resolution. *J. Mol. Biol.* **1992**, *228*, 1177–1192.
- (74) Vogel, H. J. Calmodulin: A Versatile Calcium Mediator Protein. *Biochem. Cell Biol.* **1994**, *72*, 357–376.
- (75) James, P.; Vorherr, T.; Carafoli, E. Calmodulin-Binding Domains: Just Two Faced or Multi-Faceted? *Trends Biochem. Sci.* **1995**, *20*, 38–42.
- (76) Ikura, M. Calcium Binding and Conformational Response in EF-Hand Proteins. *Trends Biochem. Sci.* **1996**, *21*, 14–17.
- (77) Babu, Y. S.; Sack, J. S.; Greenhough, T. J.; Bugg, C. E.; Means, A. R.; Cook, W. J. Three-Dimensional Structure of Calmodulin. *Nature* **1985**, *315*, 37–40.
- (78) Seaton, B.; Head, J.; Engelman, D.; Richards, F. Calcium-Induced Increase in the Radius of Gyration and Maximum Dimension of Calmodulin Measured by Small-Angle X-ray Scattering. *Biochemistry* **1985**, *24*, 6740–6743.
- (79) Kuboniwa, H.; Tjandra, N.; Grzesiek, S.; Ren, H.; Klee, C. B.; Bax, A. Solution Structure of Calcium-Free Calmodulin. *Nat. Struct. Biol.* **1995**, *2*, 768–776.
- (80) Zhang, M.; Tanaka, T.; Ikura, M. Calcium-Induced Conformational Transition Revealed by the Solution Structure of Apo Calmodulin. *Nat. Struct. Biol.* **1995**, *2*, 758–767.
- (81) Finn, B. E.; Evenäs, J.; Drakenberg, T.; Waltho, J. P.; Thulin, E.; Forsén, S. Calcium-Induced Structural Changes and Domain Autonomy in Calmodulin. *Nat. Struct. Biol.* **1995**, *2*, 777–783.
- (82) Andersson, T.; Drakenberg, T.; Forsen, S.; Thulin, E. Characterization of the Ca²⁺ Binding Sites of Calmodulin from Bovine Testis Using 43Ca and 113Cd NMR. *Eur. J. Biochem.* **1982**, *126*, 501–505.
- (83) Babu, Y. S.; Bugg, C. E.; Cook, W. J. Structure of Calmodulin Refined at 2.2 Å Resolution. *J. Mol. Biol.* **1988**, *204*, 191–204.
- (84) Moree, B.; Connell, K.; Mortensen, R. B.; Liu, C. T.; Benkovic, S. J.; Salafsky, J. Protein Conformational Changes are Detected and Resolved Site Specifically by Second-Harmonic Generation. *Biophys. J.* **2015**, *109*, 806–815.
- (85) Vanzi, F.; Sacconi, L.; Cicchi, R.; Pavone, F. S. Protein Conformation and Molecular Order Probed by Second-Harmonic-Generation Microscopy. *J. Biomed. Opt.* **2012**, *17*, 060901.
- (86) Papish, A. L.; Tari, L. W.; Vogel, H. J. Dynamic Light Scattering Study of Calmodulin–Target Peptide Complexes. *Biophys. J.* **2002**, *83*, 1455–1464.
- (87) Muthukumar, M. *Polymer Translocation*; CRC Press: Boca Raton, FL, 2011.
- (88) Meller, A.; Branton, D. Single Molecule Measurements of DNA Transport Through a Nanopore. *Electrophoresis* **2002**, *23*, 2583–2591.
- (89) Smoluchowski, M. V. Attempt on a Mathematical Theory for Coagulation Kinetics. *Z. Phys. Chem.* **1917**, *92*, 129–168.
- (90) Larkin, J.; Henley, R.; Bell, D. C.; Cohen-Karni, T.; Rosenstein, J. K.; Wanunu, M. Slow DNA Transport Through Nanopores in Hafnium Oxide Membranes. *ACS Nano* **2013**, *7*, 10121.
- (91) Wanunu, M.; Dadosh, T.; Ray, V.; Jin, J. M.; McReynolds, L.; Drndic, M. Rapid Electronic Detection of Probe-Specific microRNAs Using Thin Nanopore Sensors. *Nat. Nanotechnol.* **2010**, *5*, 807–814.
- (92) van Thor, J. J.; Pierik, A. J.; Nugteren-Roodzant, I.; Xie, A.; Hellingwerf, K. J. Characterization of the Photoconversion of Green Fluorescent Protein with FTIR Spectroscopy. *Biochemistry* **1998**, *37*, 16915–16921.
- (93) Wolf-Watz, M.; Thai, V.; Henzler-Wildman, K.; Hadjipavlou, G.; Eisenmesser, E. Z.; Kern, D. Linkage Between Dynamics and Catalysis in a Thermophilic-Mesophilic Enzyme Pair. *Nat. Struct. Mol. Biol.* **2004**, *11*, 945–949.

NOTE ADDED AFTER ASAP PUBLICATION

This paper posted ASAP on 5/9/2017. Part C of Figure 2 and related text were corrected, and the revised version was reposted on 5/11/2017.